ORIGINAL PAPER

Graphene/poly(*ortho*-phenylenediamine) nanocomposite material for electrochemical supercapacitor

H. Yadegari · H. Heli · A. Jabbari

Abstract Reduced graphene oxide was synthesized by simple chemical processing of graphite. Electron microscopy investigations of synthesized graphene showed slightly folded transparent sheets with a few square micrometers dimension. Poly(*ortho*-phenylenediamine)/graphene/Pt electrode was electrochemically fabricated in a 2.0-M H_2SO_4 solution by means of multiple potential cycling. Due to the catalytic effect of graphene on the oxidative electropolymerization of *ortho*-phenylenediamine, the *ortho*-phenylenediamine/graphene (P*o*PD/GR) nanocomposite showed greatly enhanced electrical properties and excellent capacitive behavior. Electrochemical impedance spectroscopy, galvanostatic charge/discharge curves, and voltammetric investigations revealed that P*o*PD/GR nanocomposite represented good capacitive behavior with a specific capacitance as high as 308.3 F g^{-1} at 0.1 A g^{-1}. It is almost three times higher than that of pure graphene (111.7 F g^{-1}). In addition, the nanocomposite electrode retained more than 99 % of the initial capacity after 1,500 cycles at a current density of 1 A g^{-1}.

Keywords Nanocomposite material · Conducting polymer · Electrochemical properties · Electrochemical supercapacitor

Introduction

There are enormous attentions to renewable energy resources today more than ever, in response to the growing concern over global warming as well as depletion of fossil fuel resources. Accordingly, high capability energy saving devices are needed to restore electric energy when it is available and recover it at another time. Batteries have been the technology of choice for these applications because of their high volumetric and gravimetric energy density. However, most types of batteries suffer from poor cycle and shelf life. At the same time, alternative energy storage systems, supercapacitors, are able to store and deliver energy at relatively high power densities with long cycle life [1, 2]. There are two basic types of supercapacitor depending on charge-storage mechanism: (1) electrical double-layer capacitors based on high-area carbon materials [3], such as activated carbons [4], carbon black [5], carbon aerogels [6], carbon nanotubes [7], mesoporous carbons [8], carbon composites [9], and graphene nanosheets [2, 10]; and (2) redox supercapacitors based on transition metal oxides [11–16] and conducting polymers [17, 18].

Electrically conducting polymers and their composites are among the most promising materials for fabrication of high-performance supercapacitors [19], due to the good intrinsic conductivity, low band gap, suitable morphology, fast kinetics of charge/discharge processes, and low cost [20]. Polyaniline, polypyrrole, polythiophene, and their derivatives have been the most commonly studied polymers in this regard [20]. Poly(*ortho*-phenylenediamine) (P*o*PD), as one of the conductive polymers, has potential for applications in photoelectrochemistry, electrocatalysis, electrochromic displays, sensors and biosensors, corrosion suppression, as well as in batteries and supercapacitors [18, 21, 22]. P*o*PD can be prepared electrochemically in acid, neutral, and alkaline solutions, and is stable in air and aqueous solutions [23].

Recently, graphene as a form of two-dimensional sheet of sp^2-hybridized carbon is emerging as a competitive material for application in supercapacitors [18, 24], as well as in batteries [25] and solar cells [26]. Graphene possesses a variety of unique characteristics such as large thermal and

H. Yadegari (✉) · A. Jabbari
Department of Chemistry, Faculty of Science, K.N. Toosi University of Technology, P.O. Box 16315-1618, Tehran, Iran
e-mail: yadegari.hossein@gmail.com

H. Heli
Institute of Mechanics, Iranian Space Research Center, Shiraz 7155863333, Iran

electrical conductivity, superior mechanical properties, high surface area, and chemical stability [27, 28], which serves it as a promising material in these regards. On the other hand, supporting the high-rate electrochemical redox film (such as lightweight conducting polymers) on the special two-dimensional structure of graphene as nanocomposites provides both the electrochemical double-layer capacitance and the highly reversible pseudocapacitance behaviors. Hence, remarkably increase in the overall capacitance of these nancomposite materials leads to the supercapacitors with higher energy density [18, 29, 30].

It has been reported recently by Mu [31] that the reduced graphene oxide has a catalytic ability for the electrochemical oxidative polymerization of ortho-phenylenediamine (oPD), and hence, graphene can enhance the electrical properties of PoPD. In the present work, synthesis of PoPD/graphene nanocomposite and its application as an electrode material for electrochemical supercapacitors are investigated.

Experimental

Materials

Graphite fine powder (<50 μm), sulfuric acid, sodium nitrate, potassium permanganate, and hydrazine monohydrate used in this work were of analytical grade from Merck (Darmstadt, Germany) and were used without further purification. All solutions were prepared with doubly distilled water.

Synthesis of graphene

Reduced graphene oxide was synthesized from natural graphite using a modified Hummer's method [32]. In a typical synthesis process, 2.0 g of graphite was dispersed into 140 ml concentrated sulfuric acid and 1.0 g of sodium nitrate was added to the reaction vessel under an ice bath. Then, 6.0 g potassium permanganate was slowly added to the mixture and was stirred for 2 h to fully oxidize graphite into graphite oxide (GO). Afterwards, the mixture was diluted with distilled water. After that, a 5 % H_2O_2 solution was added to the mixture until the color of the mixture changed to brilliant yellow. The suspension was filtered, and the obtained GO was thoroughly washed by water. GO was then re-dispersed in distilled water and exfoliated to generate graphene oxide under ultrasound irradiation using an ultrasonic bath for 3 h. During the ultrasonication, the suspension color gradually turned to brown, and the GO powders were transformed into the GO sheets. Finally, the exfoliated GO was reduced to graphene by refluxing with hydrazine monohydrate at 100 °C for 2 h. During this reduction process, the color of the solution turned to dark black. The final product was filtered, washed by distilled water and ethanol, and dried in an oven at 80 °C.

Electrode preparation

In order to prepare the graphene/platinum (GR/Pt) electrode, graphene (90 %) was ground with polyvinylidene difluoride (10 %), and dispersed in N-methyl pyrrolidone by means of an ultrasonic bath to obtain a paste. The resulting composite was supported on a 2.0-mm diameter Pt disk electrode and then heated to 100 °C in an oven for several hours. For the preparation of PoPD/graphene/platinum (PoPD/GR/Pt) electrode, the GR/Pt electrode was transferred into a 0.1-M oPD, dissolved in 2.0 M sulfuric acid solution. Potential in the range of −100 to 1,000 mV (vs. Ag/AgCl) in a regime of cyclic voltammetry was applied for 100 cycles at a potential sweep rate of 50 mV s^{-1}. The PoPD/platinum (PoPD/Pt) electrode was fabricated by electrodeposition of the PoPD directly on a Pt electrode as described above. The mass of deposited PoPD on PoPD/GR/Pt electrode was calculated from the charge (Q) passed during characteristic cyclic voltammogram (CV) of corresponding electrode (Fig. 4, vide infra) based on the Faraday's law: $Q=znF$, where Q is the difference in passed charge through PoPD/GR/Pt and GR/Pt electrodes (net charge associated with PoPD), z is the number of exchanged electrons, and n is the number of moles [33]. Considering a value of 2 for z and 104 for oPD molecular weight, the mass of deposited PoPD on PoPD/GR/Pt electrodes was estimated. All the electrodes were rinsed thoroughly with distilled water and dried in air prior to the electrochemical experiments.

Apparatus

Electrochemical measurements were carried out in a conventional three-electrode cell which contained 2.0 M H_2SO_4 solution as supporting electrolyte which powered by a μ-Autolab potentiostat/galvanostat, type III, (Utrecht, The Netherlands). The system was run by a PC through FRA and GPES 4.9 softwares. A Pt disk and an Ag/AgCl, saturated KCl (from Metrohm) were used as counter and reference electrodes, respectively.

Scanning electron microscopy (SEM) was performed by a Model X-30 Philips scanning electron microscope (The Netherlands), and transmission electron microscopy (TEM) was performed using a CEM 902A ZEISS transmission electron microscope (Oberkochen, Germany), with an accelerating voltage of 80 kV. Samples were prepared by placing a drop of the particles, dispersed in acetone, on a carbon-covered copper grid (400 mesh) and evaporating the solvent.

Powder x-ray diffraction (XRD) patterns were measured by a Philips X'Pert (Almelo, The Netherlands) using Cu Kα

radiation at 40 kV and 30 mA in the 2θ° range from 10° to 60°. Fourier transform infrared (FTIR) spectra of KBr powder-pressed pellets having 1 wt% of sample were recorded on an ABB BOMEM model FTLA 2000 instrument.

Results and discussion

Structural investigation

The X-ray diffraction patterns of the pristine graphite and synthesized graphene are depicted in Fig. 1. The XRD pattern of the pristine graphite (curve a) shows two sharp peaks at 2θ=26.49° and 54.58°, corresponding to the (0 0 2) and (0 0 4) reflections. These are also assigned to layer-to-layer distances (d spacing) of 3.36 and 1.68 Å. In the XRD pattern of the synthesized graphene (curve b), however, a broad peak centered at 2θ=24.17°, corresponding to the (0 0 2) reflection of graphene sheets with a d spacing of 3.55 Å is observed. The broad reflection peak of graphene indicates poor ordering of the sheets and hints that the sample is composed of mostly monolayer or few layers agglomerate of graphene sheets [18, 34]. This is consistent with the data from electron microscopy (vide infra). Moreover, the relatively weak peaks in the 2θ interval of 40–50° are due to the (1 0 0) and (1 0 1) reflections, originated from more common hexagonal and coexisting rhombohedral phases, respectively.

Morphological characterizations

SEM and TEM micrographs of the as-prepared graphene are depicted in Fig. 2. SEM micrograph (Fig. 2a) shows the slightly folded paper-like structure with a few micrometers dimensions. Some of the graphene sheets tend to wrinkle

and curl together and form fluffy agglomerates. TEM micrograph (Fig. 2b) shows the entangled transparent sheets with a few square micrometers dimension. Few overlaid graphene sheets also can be obviously seen on the edges of the graphene agglomerates.

SEM micrographs of the PoPD/Pt, GR/Pt, and PoPD/GR/Pt electrodes are also shown in Fig. 2. Micrograph of the PoPD/Pt electrode (Fig. 2c) shows almost a smooth surface with particles that firmly fix on the Pt electrode and create the island-like structure. The GR/Pt electrode material (Fig. 2d) consists of paperlike graphene sheets, which slightly folded together. The micrograph of the PoPD/GR/Pt electrode (Fig. 2e) obviously shows the graphene sheets which entirely have been covered by PoPD. Moreover, the reduced size of the PoPD particles on graphene surface in comparison with the PoPD film formed on the Pt electrode surface is due to the reduction of local current density on the graphene sheets, as a result of increasing in the specific surface area of the GR/Pt electrode surface.

FTIR spectroscopy

Figure 3 shows the baseline corrected FTIR spectra of the synthesized graphene and PoPD/GR composite. In the spectrum of graphene, the broad band centered at 1,190 cm^{-1} is assigned to the C–O stretching vibrations of the phenolic and carboxylic groups of the reduced graphene oxides sheets [35]. Moreover, the peak at about 1,570 cm^{-1} can be attributed to the C=C skeletal vibration of the graphene sheets [35, 36]. In the nanocomposite spectra, the broad peak centered at 3,444 cm^{-1} is related to the N–H stretching vibrations. The peaks in the region of 1,400–1,600 cm^{-1} are ascribed to the stretching of C–H and C=C groups of the benzene ring. In addition, the band at 1,645 cm^{-1} can be assigned to the C=N stretching, which is in conjugation
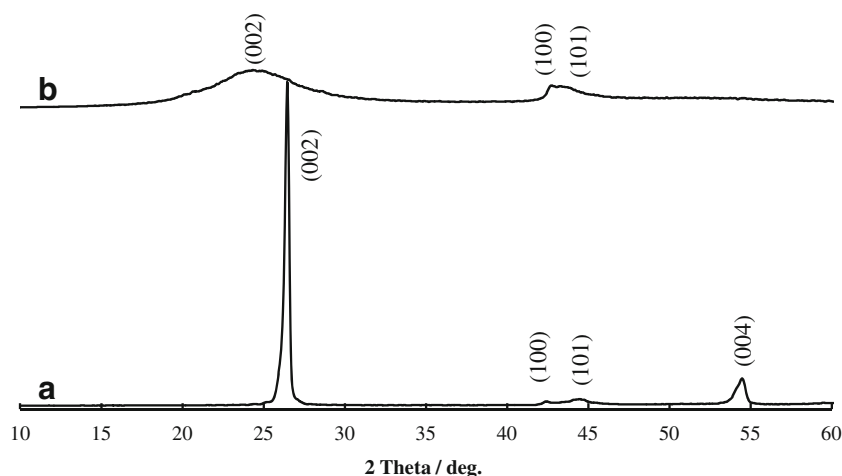

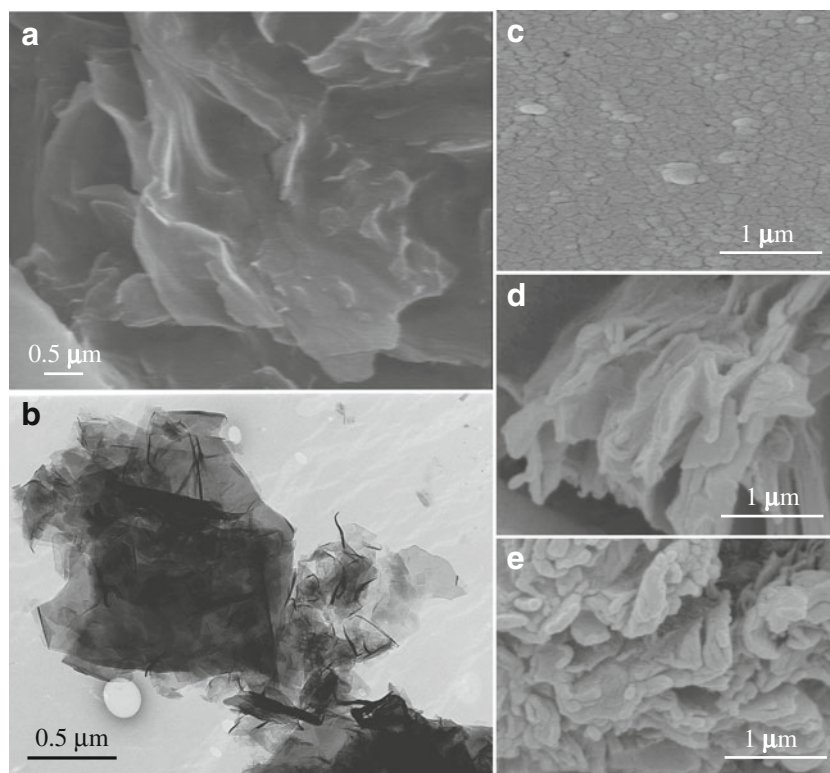Fig. 1 XRD pattern of the pristine graphite (**a**) and the synthesized graphene (**b**)

Fig. 2 SEM (**a**) and TEM (**b**) micrographs of synthesized graphene; SEM micrographs of PoPD/Pt (**c**), GR/Pt (**d**), and PoPD/GR/Pt (**e**) electrodes

with the phenyl group. The peak at 1,236 cm^{-1} is assigned to the C–N–C stretching in the benzenoid units. The FTIR results confirm that the PoPD is deposited on the GR surface.

Voltammetric investigations

Figure 4 shows the electropolymerization CVs of Pt (A) and GR/Pt (B) electrodes in 0.1 M oPD and 2.0 M sulfuric acid solution. The sharp irreversible anodic peak around 0.8 V during the first cycle in Fig. 4a is related to the oxidation of oPD monomer on Pt electrode surface. As the cycle number increases, the corresponding current of the anodic peak decreases since the Pt surface is covering by the PoPD film. On the other side, a reversible redox peak around 0.3 V related to the oxidation/reduction reaction of PoPD film is growing up, indicating that the PoPD film is forming on the Pt electrode surface. A similar behavior was observed
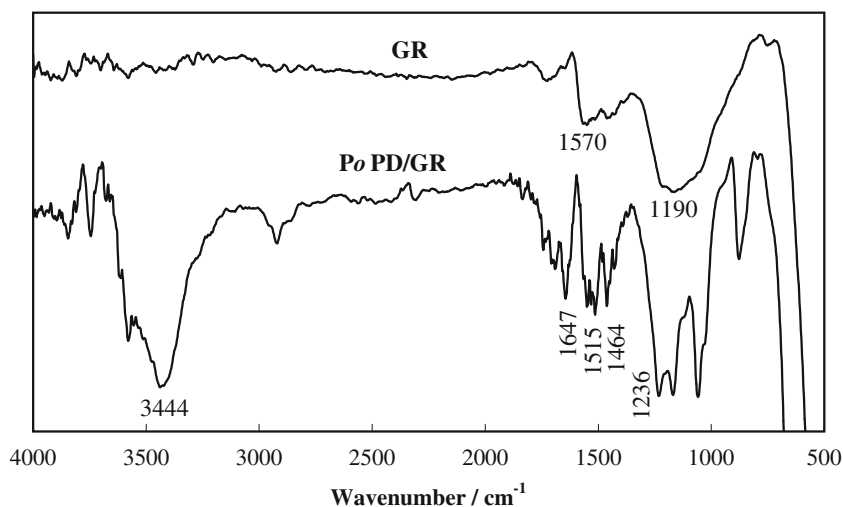

Fig. 3 Baseline corrected FTIR spectra of graphene and PoPD/GR nanocomposite
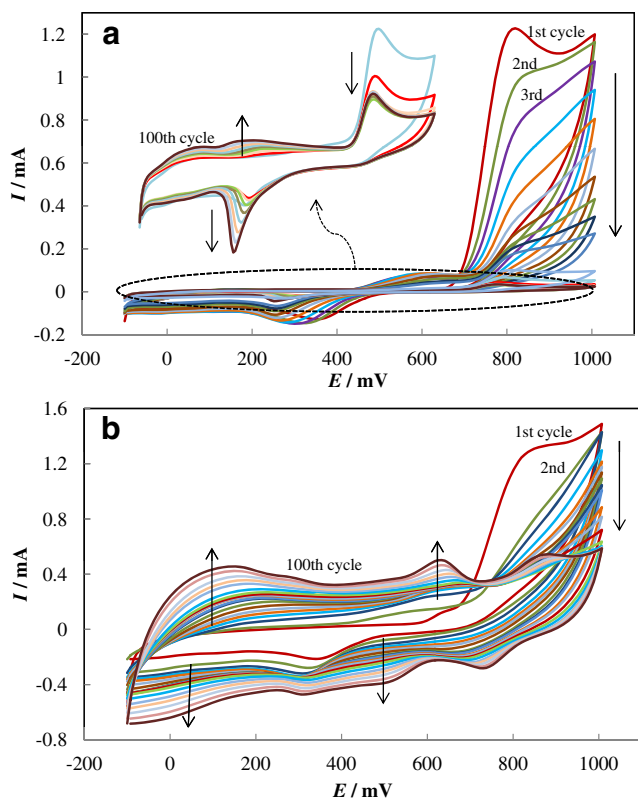
Fig. 4 Electropolymerization CVs of Pt (**a**) and GR/Pt (**b**) electrodes in 0.1 M *o*PD and 2.0 M sulfuric acid solution recorded at a potential sweep rate of 50 mV s^{-1}. (1st–10th, 15th, 20th, 30th, 40th, 50th, 60th, 70th, 80th, 90th, and 100th CVs are shown)

Fig. 5 a CVs of P*o*PD/Pt, GR/Pt, and P*o*PD/GR/Pt electrodes in an aqueous solution of 2.0 M H$_2$SO$_4$ recorded at a potential sweep rate of 50 mV s^{-1} (the potential window was −0.1–0.8 V for P*o*PD/Pt electrode and −0.2–0.8 V for GR/Pt and P*o*PD/GR/Pt electrodes). **b** CV of P*o*PD/Pt electrode with larger magnification

during consecutive CVs of GR/Pt electrode in *o*PD solution (Fig. 4b), except that the charge passed through the electrode was larger for the latter case, due to the enhanced surface area and charge transfer properties of the GR/Pt electrode. In addition, several growing redox peaks can be observed for GR/Pt electrode which is further discussed below.

CVs of P*o*PD/Pt, GR/Pt, and P*o*PD/GR/Pt electrodes recorded in 2.0 M H$_2$SO$_4$ solution in the range of −0.2-0.8 V using a potential sweep rate of 50 mV s^{-1} are shown in Fig. 5a. CV of P*o*PD/Pt electrode exhibits one oxidation and two reduction peaks (see also Fig. 5b). Similar redox behavior for P*o*PD has been reported previously [37]. Herein, the O1/R1 redox couple (at 0.11/0.08 V) is attributed to the reversible oxidation and reduction of reduced and semioxidized forms of P*o*PD; and the O1/R2 redox couple (at 0.11/0.17 V) is related to the oxidation and reduction of the semioxidized and fully oxidized forms of P*o*PD [37]. CV of GR/Pt electrode shows a rectangular shape and an excellent capacitive behavior. CV of P*o*PD/GR/Pt electrode shows three redox couples with mid-peak potentials of 0.05, 0.38, and 0.57 V. The middle couple is also accompanied by shoulder-like peaks. A similar behavior for P*o*PD deposited on the graphene surface has been observed [31]. Appearance
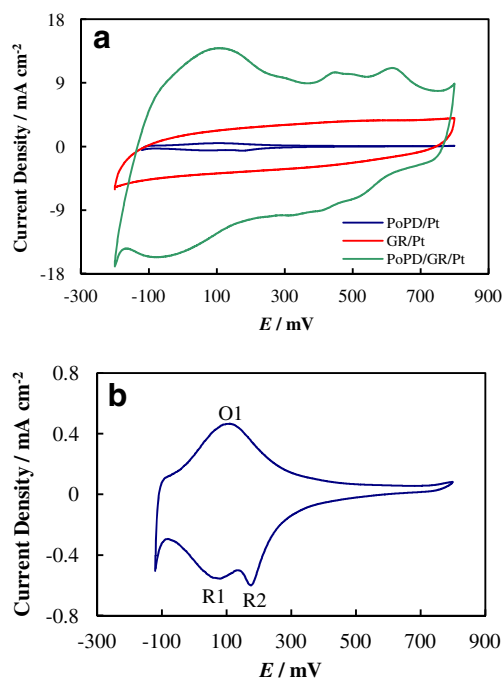
of these peaks and the shoulders may be attributed to different processes of: (1) multi-step electrode process, (2) presence of oligomers occluded in the polymer films, (3) formation of polymer fragments with different structure, (4) conformational changes in the polymers, (5) presence of polymer fragments with different conjugation length, and (6) different state of polymer in first layer adjacent to the substrate and in the film bulk [38]. The peak current and the faradaic charge of CV of P*o*PD/GR/Pt electrode are the highest, compared to the two other electrodes. Higher charge in CV of P*o*PD/GR/Pt electrode indicates an improvement in the charge transfer characteristic as well as specific capacitance of the nanocomposite. Herein, the electropolymerization reaction is initiated by free radicals of graphene sheets, and P*o*PD film is formed on the graphene surface with a ploy(aniline)-like structure [31], which is responsible for great enhancement of charge transfer and capacitive properties.

CVs of P*o*PD/Pt, GR/Pt, and P*o*PD/GR/Pt electrodes in 2.0 M H$_2$SO$_4$ solution recorded at different potential sweep rates in a wide range of 2–500 mV s^{-1} are shown in Fig. 6. CVs of P*o*PD/Pt electrode (A) exhibit well-defined peaks with the peak-to-peak (R1/O1) potential separation (at the potential sweep rate of 10 mV s^{-1}) of 0.05 V. The peak-to-peak potential separation deviated from the theoretical value of zero and slightly increases at higher potential sweep rates. This indicates a limitation in the charge-transfer kinetics
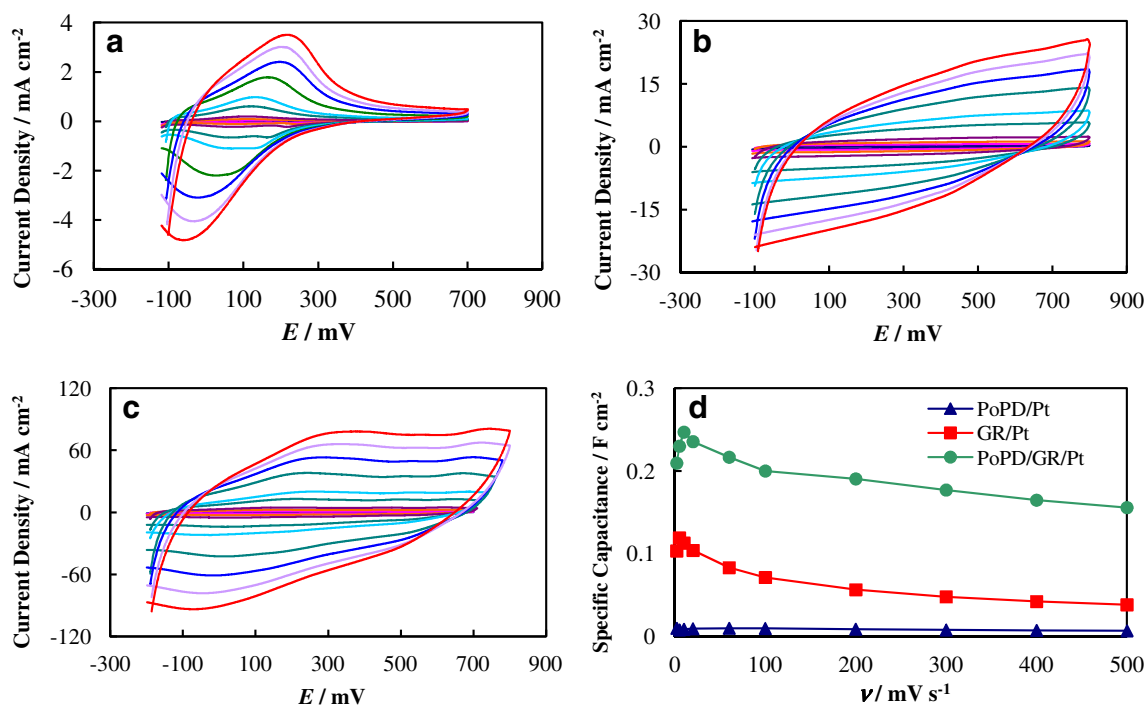
Fig. 6 CVs of PoPD/Pt (**a**), GR/Pt (**b**), and PoPD/GR/Pt (**c**) electrodes in 2.0 M H$_2$SO$_4$ solution recorded at different potential sweep rates. **d** Specific capacitances calculated from CVs of PoPD/Pt, GR/Pt, and PoPD/GR/Pt electrodes at different potential sweep rates

arising from the chemical interaction between the electrolyte ions and the modifier film, the lateral interaction of the immobilized redox couples present on the surfaces, dominated by electrostatic factors, coupled diffusion-migration processes in the bulk of film, and the presence of non-equivalent sites in the film [39]. Along with the potential sweep rate increase, the peak R2 tends to merge to peak R1, and in the potential sweep rates higher than 100 mV s^{-1} just one reduction peak is observed in the voltammograms. CVs of GR/Pt electrode (B) present a regular rectangular shape, suggesting that graphene shows a good power capability due to their uniform mesopore distribution. It can be seen that CVs of graphene retain a similar shape even at high sweep rates up to 100 mV s^{-1}, indicating an excellent capacitance behavior, low contact resistances, and the fast diffusion of electrolyte ions into the graphene sheets [40]. The CV curves tend to show a narrower loop with oblique angles at potential sweep rates up to 150 mV s^{-1}. In CVs of PoPD/GR/Pt electrode (C), along with the potential sweep rate increase, the cathodic peaks shift positively, and the anodic peaks shift negatively which is mainly due to the resistance of the electrode [41].

In the cyclic voltammetry technique, the specific capacitance per surface area, C_{SA} (Farad per square centimeter), of the electrode can be calculated according to the following equation:

$$C_{SA} = Q/AV = I\Delta t/A\Delta V = I/Av \qquad (1)$$

where I is the cathodic peak current of the voltammograms (amperes), A is the geometric surface area of the electrode (square centimeters), and ν is the potential sweep rate (volts per second). The variations of the specific capacitance of PoPD/Pt, GR/Pt, and PoPD/GR/Pt electrodes as a function of the potential sweep rate are shown in Fig. 6d. Upon increasing the potential sweep rate, the specific capacitances of all electrodes increase for a few initial points (2–10 mV s^{-1}), and then decrease (20–500 mV s^{-1}). The increase of specific capacitances at lower potential sweep rates is due to the fast increase of double layer current as a result of increasing the potential sweep rate. After that, with more increase of the potential sweep rate, the accessible pores and/or redox reaction sites decrease, and hence, the specific capacitance decreases. In addition, the capacitance of PoPD/GR/Pt electrode is much higher than the sum of the capacitance of PoPD/Pt and GR/Pt electrodes in all potential sweep rates. The greatly enhanced capacitance of PoPD/GR/Pt electrode can be related to the synergetic effect of the superior conducting and mechanical properties of graphene and high pseudocapacitance of PoPD. The synergetic effect is a result of combination between the double-layer capacitive charging of graphene and the pseudocapacitance of the faradaic redox reaction of PoPD in a way that both charge storage mechanisms work in parallel. Therefore, the overall capacitance of the composite electrode would be the sum of the double-layer capacitance and the faradaic capacitance. However, in the case of PoPD/GR/Pt electrode, the specific capacitance per surface

area of the electrode is much more than the sum of the specific capacitance of P*o*PD/Pt and GR/Pt electrodes. This outcome is due to the increase of the microscopic surface area of GR/Pt electrode in comparison with bare Pt electrode. In other words, P*o*PD/GR nanocomposite is highly loaded by P*o*PD and hence, show such enhanced specific capacitance. In fact, the synergetic effect of the nanocomposite comes from the new additional interfaces between GR and P*o*PD that can store the electric charge via double-layer mechanism. In addition, P*o*PD/GR nanocomposite presents enhanced electrode/electrolyte interface areas, high electroactive regions, and short diffusion lengths, which can ensure the high utilization of loaded P*o*PD.

Charge/discharge curves

The galvanostatic charge/discharge curves of P*o*PD/Pt, GR/Pt, and P*o*PD/GR/Pt electrodes at a constant current density of 0.16 mA cm^{-2} in the potential range of 0–0.8 V are depicted in Fig. 7a. The charge/discharge curves show a slight curvature, indicating the contribution of the faradaic redox pseudocapacitive along with the double-layer capacitance. The specific capacitance per surface area, C_{SA} (Farad per square centimeter), and specific gravimetric capacitance, C_{Sg} (Farad per gram) of the samples were estimated from the discharge process according to the following equations:

$$C_{SA} = I\Delta t/\Delta V A \tag{2}$$

$$C_{Sg} = I\Delta t/\Delta V m \tag{3}$$

where I is the discharge current (ampere), Δt is the discharge time (seconds), ΔV is the potential change during discharge process (volts), A and m are the geometric surface area (square centimeters) and the mass of active material (grams) of a single electrode, respectively. The P*o*PD film shows small specific capacitance of 0.005 F cm^{-2}, owing to the fact that the P*o*PD film has poor conductivity. The specific capacitances of GR/Pt and P*o*PD/GR/Pt electrodes were obtained as 0.17 and 0.515 F cm^{-2}, respectively. The specific capacitance of P*o*PD/GR/Pt electrode is much higher than sum of the specific capacitances of P*o*PD/Pt and GR/Pt electrodes. This great enhancement in the specific capacitance of P*o*PD/GR nanocomposite is due to the synergetic effect between graphene sheets and P*o*PD film. The catalytic effect of graphene sheets on the synthesis of the nanocomposite causes to improve the electrical and redox characteristics of P*o*PD/GR nanocomposite (vide supra) which hence improve the capacitive behavior of P*o*PD/GR nanocomposite. The specific gravimetric capacitance of GR/Pt and P*o*PD/GR/Pt electrodes based on the mass of active material was 111.7 and 308.3 F g^{-1}. The specific capacitance enhancement for P*o*PD/GR/Pt electrode in comparison with GR/Pt electrode (111.7 F g^{-1}) is arisen from electrochemical activity of P*o*PD phase.

The charge/discharge curves of P*o*PD/GR/Pt electrode in 2.0 M H$_2$SO$_4$ at different current densities of 1.0 (1.6), 2.5 (4.0), and 5.0 (8.0)A g^{-1} (milliampere per square centimeter) are depicted in Fig. 7b. The triangular feature remains even at the high current load of 5.0 A g^{-1}. This observation indicates that the capacitor based on the nanocomposite has excellent electrochemical reversibility and charge/discharge properties.

Fig. 7 **a** Galvanostatic charge/discharge curves for P*o*PD/Pt, GR/Pt, and P*o*PD/GR/Pt electrodes in 2.0 M H$_2$SO$_4$ solution at a constant current density of 0.16 mA cm^{-2}. *Inset*: The charge/discharge curve of P*o*PD/Pt electrode with larger magnification. **b** Charge/discharge curves for P*o*PD/GR/Pt electrode in 2.0 M H$_2$SO$_4$ solution at different current densities of 1.0 (1.6), 2.5 (4.0), and 5.0 (8.0)A g^{-1} (mA cm^{-2}). **c** Variation of the specific capacitance and specific energy of P*o*PD/GR/Pt electrode as a function of discharge current density. **d** Ragone plot for P*o*PD/GR/Pt electrode at various current densities from 0.1 to 5.0 A g^{-1} (current density values are depicted at each data point)
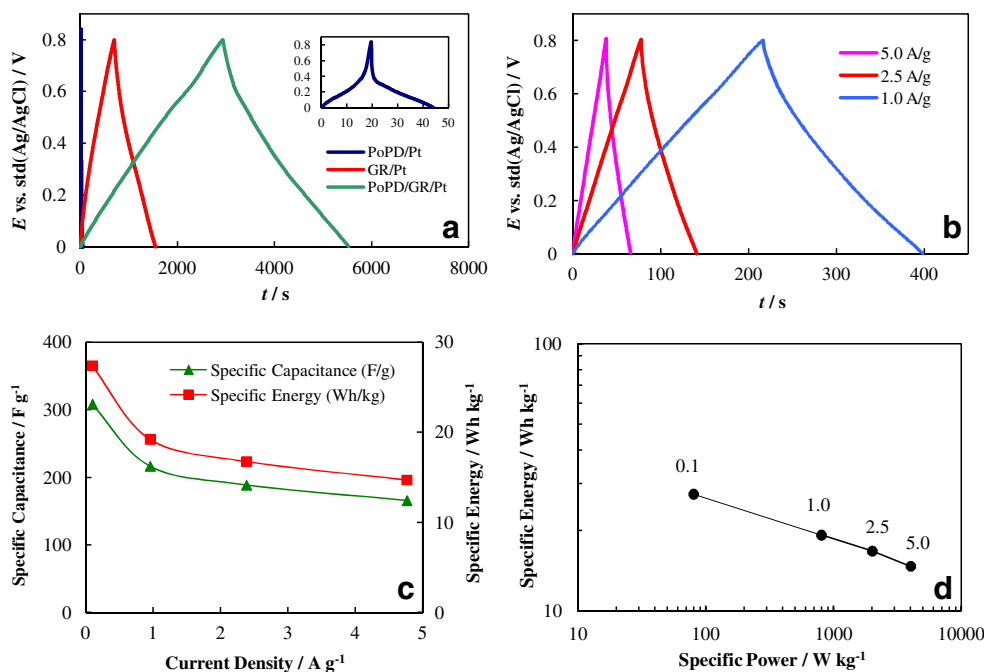
Table 1 Electrical parameter values for P*o*PD/GR/Pt electrode calculated from galvanostatic charge/discharge curves at different current densities in a three-electrode system

Current density, $A\ g^{-1}$, ($mA\ cm^{-2}$)	Discharge time (s)	Specific capacitance, $F\ g^{-1}$, ($F\ cm^{-2}$)	Specific energy, $Wh\ kg^{-1}$, ($Wh\ m^{-2}$)	Specific power, $W\ kg^{-1}$, ($W\ m^{-2}$)
0.1 (0.16)	2,590	308.3 (0.52)	27.4 (0.46)	38.1 (0.64)
1.0 (1.6)	182	216.7 (0.36)	19.3 (0.32)	381 (6.4)
2.5 (4.0)	63.5	188.8 (0.32)	16.8 (0.28)	952 (15.9)
5.0 (8.0)	27.8	165.8 (0.28)	14.7 (0.25)	1,905 (31.8)

Moreover, the Ohmic drop is not apparent, even at 5.0 A g^{-1}, indicating little overall resistance of the nanocomposite. The specific capacitance per surface area and specific gravimetric capacitance of P*o*PD/GR/Pt electrode at different current densities are reported in Table 1. A comparison of the specific capacitances of some supercapacitor electrode materials is also made in Table 2.

The maximum specific power per surface area, P_{SA} (watts per square meter), and specific gravimetric power, P_{Sg} (watts per kilogram) can be calculated from charge–discharge cycling data (Fig. 7b) in a three-electrode system using the following equations [49]:

$$P_{SA} = IV/2A \qquad (4)$$

$$P_{Sg} = IV/2m \qquad (5)$$

and the maximum specific energy per surface area, E_{SA} (watt-hour per square meter), and specific gravimetric energy, E_{Sg} (watt-hour per kilogram) can be estimated as follows:

$$E_{SA} = ItV/2A \qquad (6)$$

$$E_{Sg} = ItV/2m \qquad (7)$$

where I is the discharge current (amperes), t is the discharge time (hours), V is the operating potential window (0.8 V), A and m are the geometric surface area (square meters) and the mass of active material (kilograms) of a single electrode, respectively. The values of aforementioned electrical parameter calculated based on the galvanostatic charge/discharge curves of Fig. 7b are also presented in Table 1.

The specific gravimetric capacitance and energy of P*o*PD/GR/Pt electrode as a function of discharge current density is shown in Fig. 7c. The specific gravimetric capacitance and energy of the electrode decreases with increasing discharge current. The capacitance retention is about 54 %, with 50 times increase in current density from 0.1 to 5.0 A g^{-1}. In addition, the relation between specific energy and specific power (Ragone plot) of P*o*PD/GR/Pt electrode is shown in Fig. 7d. The nanocomposite shows good energy and power densities. For example, at a power density of 38.1 W kg^{-1}, the electrode shows energy density of 27.4 Wh kg^{-1}, and it still keeps 14.7 Wh kg^{-1} at a power density of 1.9 kW kg^{-1}.

The electrochemical stability of P*o*PD/GR nanocomposite was examined by subjecting P*o*PD/GR/Pt electrode for a long number of galvanostatic charge/discharge cycles. The cycling process was performed at a current density of 1.0 A g^{-1} for 1,500 cycles. The variation of specific capacitance as a function of cycle number is shown in Fig. 8. A little decrease in

Table 2 A comparison of the specific capacitance of some supercapacitor electrode materials

| Supercapacitor electrode material	Specific capacitance ($F\ g^{-1}$)	Loaded mass	Current density ($A\ g^{-1}$)	References
Single-walled carbon nanotube	20	–	–	[42]
Exfoliated multi-walled carbon nanotube	165	1 mg cm^{-2}	0.5	[43]
Graphene	117	5 mg	–	[10]
Graphene nanosheet	150	4 mg cm^{-2}	0.1	[44]
Graphene/multiwalled carbon nanotube	265	5 mg	0.1	[45]
Graphene-polypyrrole nanocomposite	165	–	1	[46]
Graphene-polyaniline nanocomposite	400	–	0.001	[47]
Graphene-polyaniline nanofiber	480	5 mg	0.1	[18]
Graphene-poly(*o*-aminophenol) nanocomposite	281	1.8 mg cm^{-2}	0.1	[48]
Graphene-poly(*o*-phenylenediamine) nanocomposite	308	1.7 mg cm^{-2}	0.1	This work
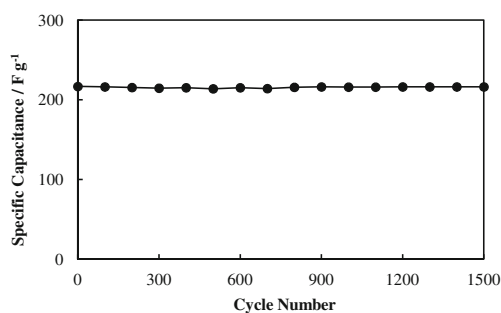
Fig. 8 Variation of the specific gravimetric capacitance of PoPD/GR/Pt electrode as a function of cycle number measured in 2.0 M H$_2$SO$_4$ solution at a current density of 1.0 A g^{-1} (1.6 mA cm^{-2})

specific capacitance is observed during consecutive cycles, and it retains more than 99 % of the initial capacitance after 1,500 cycles. As expected for pseudocapacitance reactions, the charge and discharge processes do not seem to induce significant electrochemical or structural changes in PoPD/GR/Pt electrode. The long-term stability suggests that PoPD/GR nanocomposite is a good candidate as a material for supercapacitor electrodes.

Electrochemical impedance spectroscopy

Nyquist diagrams recorded using PoPD/Pt, GR/Pt, and PoPD/GR/Pt electrodes at open circuit potential (OCP) in the frequency range of 500 KHz to 5 mHz are shown in Fig. 9. An electrical equivalent compatible with these Nyquist diagrams is also represented in Scheme 1. In this circuit, ESR is the equivalent series resistance of the electrodes, CPE$_{dl}$ is a constant phase element indicating the double-layer capacitor, R_{ct} is the charge transfer resistance, and W_o is the short-terminus Warburg impedance. The Z' axis intercept of the Nyquist plot reveals ESR, which are
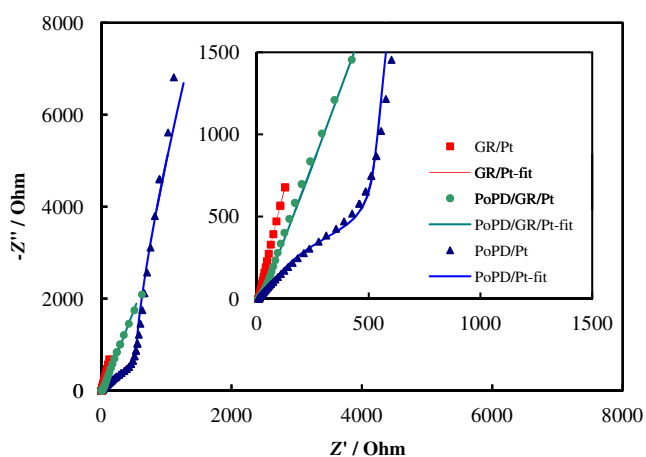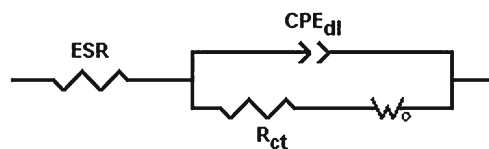

Fig. 9 Nyquist diagrams for PoPD/Pt, GR/Pt, and PoPD/GR/Pt electrodes recorded at OCP in the frequency range of 500 kHz to 0.005 Hz. The high-frequency region is depicted with higher magnification as an *inset*

Scheme 1 An electrical equivalent compatible with the Nyquist diagrams presented in Fig. 9

almost equal for all electrodes at about 7 Ω. Nyquist diagram recorded using PoPD/Pt electrode represented a semicircle over the high frequency range and a straight 45° sloped line in the medium frequency region followed by an almost vertical line in the low frequency end. The large semicircle observed for PoPD/Pt electrode indicates the high interfacial charge-transfer resistance, which can be attributed to the poor electrical conductivity of PoPD film. The 45° sloped portion of the Nyquist plot is typical of Warburg impedance and is a result of the frequency dependence of ion transport in the polymer film. The high frequency semicircle, however, is not appeared in the Nyquist diagrams recorded using GR/Pt and POAP/GR/Pt electrodes as a result of low interfacial resistance between graphene sheets and the electrode surface, and also, between graphene sheets and PoPD film [18]. On the other hand, PoPD/GR composite had lower charge-transfer resistance, compared to pure PoPD film, because PoPD film was uniformly distributed on the highly conductive graphene sheets. Moreover, the short Warburg region of the Nyquist plot of PoPD/GR/Pt electrode suggests that the electrochemical reaction of the composite electrode was a surface reaction, namely it has short ion diffusion path and the electrolyte ions do not penetrate into the bulk of PoPD film. At low frequencies, the imaginary part of the impedance curves approached nearly a vertical line in all electrodes, indicating an ideal capacitive behavior [40].

Conclusion

Reduced graphene oxide was synthesized using a simple chemical processing of graphite. A composite of PoPD with graphene was prepared by in situ electrochemical polymerization. The morphology and structure of the prepared graphene were characterized by SEM, TEM, and XRD techniques. It was demonstrated by CV that the prepared composite exhibits good electrochemical behavior for application as supercapacitor material. Due to the synergetic effect between PoPD and graphene as a result of enhanced electrochemical kinetics of mass and charge transfer into the synthesized nanostructured composite, it exposed high specific capacitance of 308.3 F g^{-1} at a current density of 0.1 A g^{-1} and good cycling stability.

References

1. Pandolfo AG, Hollenkamp AF (2006) J Power Sources 157:11–27
2. Meryl SD, Sungjin P, Yanwu Z, Jinho A, Rodney RS (2008) Nano Lett 8:3498–3502
3. Frackowiak E, Beguin F (2001) Carbon 39:937–950
4. Qu D, Shi H (1998) J Power Sources 74:99–107
5. Toupin M, Belanger D, Hill I, Quinn D (2005) J Power Sources 140:203–210
6. Probstle H, Schmitt C, Fricke J (2002) J Power Sources 105:189–194
7. Emmenegger C, Mauron P, Sudan P, Wenger P, Hermann V, Gallay R, Zuettel A (2003) J Power Sources 124:321–329
8. Numao S, Judai K, Nishijo J, Mizuuchi K, Nishi E (2009) Carbon 47:306–312
9. Sattarahmady N, Parsa A, Heli H (2013) J Mater Sci 48:2346–235
10. Yongchao S, Edward TS (2008) Chem Mater 20:6792–6797
11. Toupin M, Brousse T, Belanger D (2004) Chem Mater 16:3184–3190
12. Sugimoto W, Iwata H, Yasunaga Y, Murakami Y, Takasu Y (2003) Angew Chem Int Ed 42:4092–4096
13. Kim HK, Seong TY, Lim JH (2001) J Power Sources 102:167–171
14. Zheng MB, Cao J, Liao ST, Liu JS, Chen HQ, Zhao Y, Dai WJ, Ji GB, Cao JM, Tao J (2009) J Phys Chem C 113:3887–3894
15. Nam KW, Kim KB (2002) J Electrochem Soc 149:A346–A354
16. Kim HS, Popov BN (2003) J Electrochem Soc 150:D56–D62
17. Wang K, Huang J, Wei Z (2010) J Phys Chem C 114:8062–8067
18. Zhang K, Zhang LL, Zhao XS, Wu J (2010) Chem Mater 22:1392–1401
19. Peng C, Zhang S, Jewell D, Chen GZ (2008) Prog Nat Sci 18:777–788
20. Snook GA, Kao P, Best AS (2011) J Power Sources 196:1–12
21. Diaz AF, Nguyen MT, Leclerc M (1995) In: Rubinstein I (ed) Physical electrochemistry. Marcel Dekker, New York
22. Chen J, Liu Y, Minett AI, Lynam C, Wang J, Wallace GG (2007) Chem Mater 19:3595–3597
23. Dai HP, Wu QH, Sun SG, Shiu KK (1998) J Electroanal Chem 456:47–59
24. Wang Y et al (2009) J Phys Chem C 113:13103–13107
25. Yoo E, Kim J, Hosono E, Zhou H, Kudo T, Honma I (2008) Nano Lett 8:2277–2282
26. Wang X, Zhi LJ, Mullen K (2008) Nano Lett 8:323–327
27. Geim AK, Novoselov KS (2007) Nat Mater 6:183–191
28. Novoselov KS, Geim AK, Morozov SV, Jiang D, Katsnelson MI, Grigorieva IV, Dubonos SV, Firsov AA (2005) Nature 438:197–200
29. Wang DW, Li F, Zhao JP, Ren WC, Chen ZG, Tan J, Wu ZS, Gentle I, Lu GQ, Cheng HM (2009) ACS Nano 3:1745–1752
30. Li C, Shi G (2012) Electrochim Acta 56:10737–10743
31. Mu S (2011) Electrochim Acta 56:3764–3772
32. Hummers WS, Offeman RE (1958) J Am Chem Soc 80:1339–1339
33. Suppes GM, Deore BA, Freund MS (2008) Langmuir 24:1064–1069
34. Murugan AV, Muraliganth T, Manthiram A (2009) Chem Mater 21:5004–5006
35. Wang Y, Liu J, Liu L, Sun D (2011) Nanoscale Res Lett 6:241–248
36. Shen J, Hu Y, Shi M, Lu X, Qin C, Li C, Ye M (2009) Chem Mater 21:3514–3520
37. Bilal S, Holze R (2006) Electrochim Acta 52:1247–1257
38. Shah AA, Holze R (2006) J Electroanal Chem 597:95–102
39. Heli H, Yadegari H (2010) Electrochim Acta 55:2139–2148
40. Conway BE (1999) Electrochemical supercapacitors: scientific fundamentals and technological applications. Kluwer Academics/Plenum, New York
41. Wang YG, Li HQ, Xia YY (2006) Adv Mater 18:2619–2623
42. Ruch PW, Kötz R, Wokaun A (2009) Electrochim Acta 54:4451–4458
43. Wang G, Ling Y, Qian F, Yang X, Xi X, Li LY (2011) J Power Sources 196:5209–5214
44. Du X, Guo P, Song H, Chen X (2010) Electrochim Acta 55:4812–4819
45. Lua X, Dou H, Gao B, Yuan C, Yang S, Hao L, Shen L, Zhang X (2011) Electrochim Acta 56:5115–5121
46. Biswas S, Drzal LT (2010) Chem Mater 22:5667–5671
47. Basnayaka PA, Ram MK, Stefanakos EK, Kumar A (2013) Electrochim Acta 92:376–382
48. Heli H, Yadegari H, Jabbari A (2012) Mater Chem Phys 134:21–25
49. Gupta V, Miura N (2005) Electrochem Solid State Lett 8:A630–A632